JACS
JOURNAL OF THE AMERICAN CHEMICAL SOCIETY

Article

pubs.acs.org/JACS

Mechanistic Investigation of Water Oxidation Catalyzed by Uniform, Assembled MnO Nanoparticles

Kyoungsuk Jin,[†,#] Hongmin Seo,[†,#] Toru Hayashi,[‡,§,#] Mani Balamurugan,[†] Donghyuk Jeong,[∥] Yoo Kyung Go,[∥] Jung Sug Hong,[†] Kang Hee Cho,[†] Hirotaka Kakizaki,[‡,§] Nadège Bonnet-Mercier,[§] Min Gyu Kim,[⊥] Sun Hee Kim,[∥] Ryuhei Nakamura,[*,§] and Ki Tae Nam[*,†]

[†]Department of Materials Science and Engineering, Seoul National University, Seoul 151-742, Korea

[‡]Department of Applied Chemistry, The University of Tokyo, 7-3-1 Hongo, Bunkyo-ku, Tokyo 113-8656, Japan

[§]Biofunctional Catalyst Research Team, RIKEN Center for Sustainable Resource Science (CSRS), 2-1 Hirosawa, Wako, Saitama 351-0198, Japan

[∥]Western Seoul Center, Korea Basic Science Institute (KBSI), 150, Bukahyeon-ro, Seodaemun-gu, Seoul 120-140, Korea

[⊥]Pohang Accelerator Laboratory, Pohang University of Science and Technology (POSTECH), Pohang 790-784, Korea

Supporting Information

ABSTRACT: The development of active water oxidation catalysts is critical to achieve high efficiency in overall water splitting. Recently, sub-10 nm-sized monodispersed partially oxidized manganese oxide nanoparticles were shown to exhibit not only superior catalytic performance for oxygen evolution, but also unique electrokinetics, as compared to their bulk counterparts. In the present work, the water-oxidizing mechanism of partially oxidized MnO nanoparticles was investigated using integrated in situ spectroscopic and electrokinetic analyses. We successfully demonstrated that, in contrast to previously reported manganese (Mn)-based catalysts, Mn(III) species are stably generated on the surface of MnO nanoparticles via a proton-coupled electron transfer pathway. Furthermore, we confirmed as to MnO nanoparticles that the one-electron oxidation step from Mn(II) to Mn(III) is no longer the rate-determining step for water oxidation and that Mn(IV)═O species are generated as reaction intermediates during catalysis.

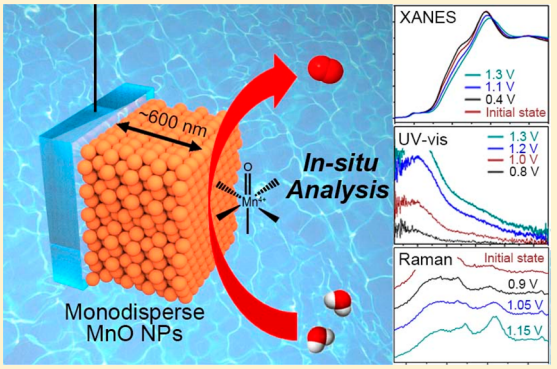

INTRODUCTION

Electrochemical water splitting to produce hydrogen and oxygen molecules is a promising process for the storage of renewable energy as chemical fuels.[1,2] Hydrogen energy is an attractive alternative resource to fossil fuels due to its high energy density and environmentally friendly characteristics. As compared to conventional gas reforming processes, electrochemical water splitting is a more efficient pathway to produce hydrogen gas and also does not generate any undesirable byproducts. However, the slow reaction kinetics for anodic oxygen evolution reaction (OER) has been a major bottleneck for the overall efficiency of the water splitting reaction.[3−5]

For the OER to proceed, four electrons and four protons must be extracted from two water molecules, a process that typically requires high overpotential. Noble metal catalysts, such as IrO_x and RuO_2, are highly active and extensively used.[6−8] However, due to the high cost of noble metals, first-row-transition-metal-based catalysts have been widely investigated for use in practical applications. In particular, various cobalt (Co)-,[9−11] iron (Fe)-,[12−14] nickel (Ni)-,[15,16] and manganese (Mn)-based[17−22] compounds were shown to exhibit good catalytic activity under basic conditions. Meanwhile, the research on the development of active catalysts operating at neutral pH is relatively insufficient. Although several transition-metal-based catalysts have been investigated at near-neutral pH,[15,23,24] performance is not good enough for practical application. Thus, substantial research efforts are required.

In nature, the water oxidation complex (WOC) of Photosystem II efficiently catalyzes the OER under neutral conditions.[25] The WOC consists of a cluster composed of manganese and calcium elements (Mn_4Ca) and its unique ligand environment, and mediates the OER with a markedly higher turnover frequency[26] and lower overpotential than have been achieved to date by synthetic catalysts.

Inspired by the WOC of Photosystem II, Mn-based catalysts have received considerable interest. Despite the development of several promising Mn-based catalytic materials, severe activity discrepancies exist between synthetic catalysts and the WOC under neutral conditions. Synthetic Mn catalysts typically require an overpotential of 500−700 mV for the OER to

Received: October 14, 2016
Published: December 28, 2016

DOI: 10.1021/jacs.6b10657
J. Am. Chem. Soc. 2017, 139, 2277−2285

proceed at neutral pH.[27−30] To overcome these issues, a better understanding of the mechanisms underlying the activity of Mn-based catalysts for the OER is required.

It has been discussed that the activity of Mn-based catalysts is mainly determined by structural parameters related to the binding of reactant adsorbates.[19,31,32] Specifically, it was reported that Mn−Mn/Mn−O local distances affect the binding strength between surface metal sites and anionic perhydroxyl or hydroxyl reaction intermediates.[32] For example, Mn_2O_3 and Mn_3O_4, which have moderate Mn−Mn/Mn−O bonding lengths, exhibited higher catalytic performance for the OER than did other Mn oxides.[32] It was also reported that the electronic configuration of the 3d orbital influences the activity of Mn-based catalysts.[33−35] Because the e_g orbital participates in σ bonding with anionic adsorbates, occupancy of this orbital directly determines the binding energy of reactant species and results in a volcano-shaped activity curve. For the OER, e_g^1 was suggested to be the optimal electronic configuration for transition-metal-based catalysts.[33−35] In this context, it has been also verified that Mn(III) species, with the electronic configuration of $t_{2g}^3e_g^1$, play crucial roles in water oxidation catalysis (vide infra).

Furthermore, investigation of the detailed mechanisms and verification of the rate-determining step (RDS) in the OER is another important research direction. The two main proposed mechanisms of O−O bond formation, generally regarded as the RDS in the OER, are the acid (electrophilic)−base (nucleophilic) (AB) and radical coupling (RC) mechanisms. The AB mechanism was proposed by the Shannon and Frei groups based on the results of electron paramagnetic resonance (EPR) and in situ FT-IR analyses. In this mechanism, octahedral metal sites act as mononuclear active species, in conjunction with adjacent proton-accepting metal species for the nucleophilic attack of water molecules, resulting in the generation of peroxo intermediates.[36,37] More recently, a direct RC pathway was proposed by the Voorhis group. On the basis of computational analyses of the mechanism of the OER by a Co oxide catalyst, dinuclear O−O bond formation by adjacent Co−oxo species was predicted to be the most energetically favorable reaction step.[38] The ligand field and specific geometry of the active metal are also reported as important determinants of the reaction pathway.[39]

Under neutral pH conditions, Mn-oxide-based catalysts show markedly reduced activity as compared to alkaline conditions. We have demonstrated that the instability of surface Mn(III) species and the symmetrical structure of Mn oxides are the main reasons for the suppressed redox capability of Mn oxides.[27,40] The stability of Mn(III) ($t_{2g}^3e_g^1$) is strongly influenced by Jahn−Teller (J−T) distortion and charge disproportionation, which are competitive reactions.[23,40,41] However, J−T distortion, which requires concomitant elongation and compression of MnO_6 octahedra, is markedly prohibited by the rigid framework of Mn oxides. Thus, charge disproportionation is favored. The introduction of asymmetry in Mn oxide catalysts was attempted by the introduction of nitrogen ligands, resulting in the suppression of charge disproportionation and enhanced activity for the OER in neutral conditions.[40,42] Additionally, it has been reported that the Mn oxide materials could be converted into active Mn(III)-containing layered structure by oxidative treatment.[17,43,44] The importance of Mn(III) for the activity of Mn oxides for the OER in neutral conditions was also exemplified by the study of amorphized Mn oxides,[17,31] Mn oxides with noble metal substrates,[45] electrodeposited Mn oxides,[23] and a comparative study of Mn oxides.[32]

We previously demonstrated that intermediate Mn(III) species can be stabilized if sufficient structural flexibility is introduced into the Mn oxide. Specifically, phosphorus-derived Mn catalysts with asymmetric Mn geometry displayed performance superior to that of oxide compounds.[20] The OER activity was assessed by measuring the applied inner pressure and local pair distribution function of the Mn(III) states. Computation analysis revealed that, although high inner pressure was required for the increased catalytic activity, J−T distortion occurred freely at Mn(III) sites in the Mn(II)O rocksalt structure. On the basis of these findings, we recently developed sub-10 nm-sized partially oxidized Mn oxide nanoparticles (MnO NPs), which exhibited higher activity under neutral pH than cobalt−phosphate (Co−Pi) amorphous films.[46] Additionally, a clear dependency of the onset potential for the OER on the particle size was observed, and the activity of the nanosized Mn oxide compounds was superior to that of bulk counterparts.[46,47] We further revealed the nanosize effect of the MnO NPs that stabilized Mn(III) species on the surface even during electrolysis. Moreover, catalytic stability of the MnO NPs was also confirmed under neutral conditions.[46,47]

Here, to understand the effects and determine the OER mechanism mediated by nanosized Mn oxides, we conducted in situ spectroscopic and electrokinetic analyses. Specifically, from the EPR, in situ X-ray absorption near edge structure (XANES), UV−vis, and Raman analysis, we successfully demonstrated a new catalytic cycle, which is exclusively applied to our Mn oxide nanoparticle system.

RESULTS AND DISCUSSION

The synthesis of the MnO NPs and preparation of electrodes were performed following a previously reported method.[46] As shown in Figure 1a and b, monodispersed 10 nm-sized MnO

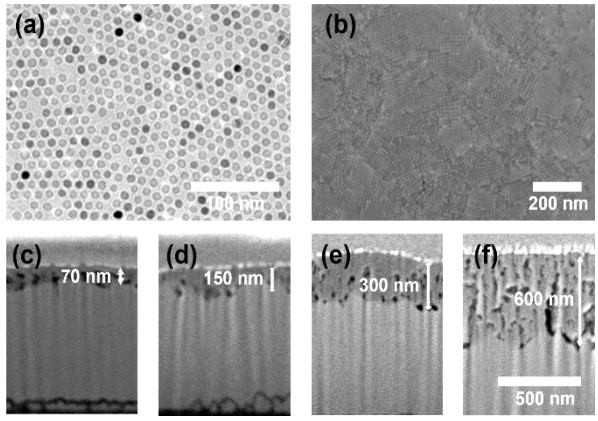

Figure 1. Electron microscopic images of MnO NP films. (a) TEM image of synthesized MnO NPs and (b) plane and (c−f) cross-sectional SEM images of MnO NPs films on FTO substrates.

NPs were successfully synthesized and loaded onto fluorine-doped tin oxide (FTO) substrates. The thickness of the MnO NP films ranged from 70 to 600 nm (Figure 1c−f) and was precisely controlled using spin coating. The detailed electrode preparation methods are provided in the Supporting Information.

The electrode kinetics of the OER by the MnO NPs were analyzed using various electrochemical techniques. Thickness-

DOI: 10.1021/jacs.6b10657
J. Am. Chem. Soc. 2017, 139, 2277−2285

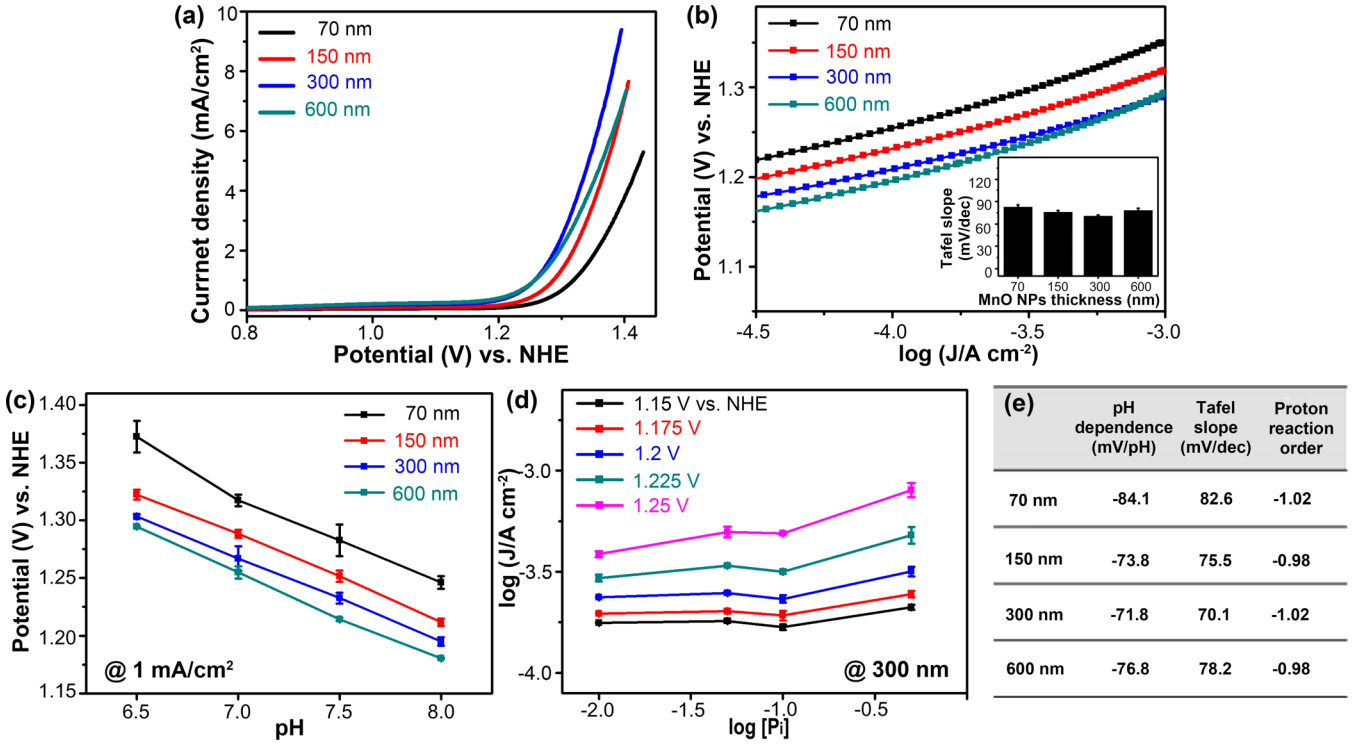

(e)

	pH dependence (mV/pH)	Tafel slope (mV/dec)	Proton reaction order
70 nm	-84.1	82.6	-1.02
150 nm	-73.8	75.5	-0.98
300 nm	-71.8	70.1	-1.02
600 nm	-76.8	78.2	-0.98

Figure 2. Electrokinetic analysis of the MnO NP films. (a) Polarization-corrected cyclic voltammetry curves, (b) Tafel plots near the onset potential, (c) pH dependency over a neutral pH range, (d) dependency of current density on phosphate concentration, and (e) a summary table for the estimated proton reaction orders of the MnO NP films of various thicknesses.

dependent water oxidizing activity was evaluated by cyclic voltammetry (CV) in 0.5 M phosphate buffer at pH 7. To minimize the contribution of non-Faradaic current, all CV curves were polarization-corrected.[24] As shown in Figure 2a, the overpotential at the current density of 5 mA/cm^2 was 610, 560, 530, and 550 mV for the 70, 150, 300, and 600 nm-thick films, respectively. We found that the 300 nm-thick films exhibited the highest water oxidation performance at 5 mA/cm^2 and that, as the film thickness exceeded 300 nm, the catalytic activity was markedly reduced. The decrease in catalytic activity for the 600 nm film was attributed to the increased charge transport limitations, which were more dominant than the increase in active sites and resulted in the saturation of the catalytic current.

Tafel plots for each of the prepared films were obtained from the polarization-corrected CV curves. The Tafel slopes measured using 70, 150, 300, and 600 nm-thick electrodes were 82.6, 75.5, 70.1, and 78.2 mV/dec, respectively (Figure 2b). For the electrochemical OER, the current−potential relationship was described by eq 1, where i_0, α, F, E^0, and b are the exchange current density, transfer coefficient, Faraday constant, thermodynamic equilibrium potential, and Tafel slope, respectively. Additionally, the Tafel slope (b) can be expressed as being inversely related to the transfer coefficient (eq 2).[48,49]

$$i = i_0 \cdot \exp\left(-\frac{\alpha(E - E^0)\mathrm{F}}{RT}\right) \quad (1)$$

$$b = \left(\frac{\partial E}{\partial \log i}\right) = \frac{2.3RT}{\alpha F} \quad (2)$$

The Tafel slopes of 70−80 mV/dec for the prepared MnO NP films corresponded to 2.3 RT/F, which indicates that the transfer coefficient was 1 and that a reversible one-electron transfer process occurred prior to the rate-determining step (RDS).[49−51]

The pH dependence of the catalytic activity of the MnO NPs was further examined under neutral conditions (Figures 2c and S1). The potentials at the current density of 1 mA/cm^2 were measured from pH 6.5 to 8.0 for each film thickness. As shown in Figure 2c, a linear relationship between pH and the measured potential was observed. The slopes were estimated to be −84.1, −73.8, −71.8, and −76.8 mV/pH for the 70, 150, 300, and 600 nm-thick MnO NP films, respectively. As was observed for the Tafel slopes, the slopes had similar values of approximately 70−80 mV/pH regardless of the film thickness. In the electrochemical rate law, the reaction order of proton is defined as $-(\partial \log j/\partial \mathrm{pH})_{E,T,P}$. Thus, using the values of the Tafel slopes and pH-dependent potential changes, the reaction order of proton can be derived from the following partial differential equation:[48,49]

$$\left(\frac{\partial E}{\partial \mathrm{pH}}\right)_{j,T,P} = -\left(\frac{\partial E}{\partial \log j}\right)_{\mathrm{pH},T,P}\left(\frac{\partial \log j}{\partial \mathrm{pH}}\right)_{E,T,P} \quad (3)$$

As shown in Figure 2e, the proton reaction order for each thickness of film was maintained as −1, which indicated inverse first-order dependence of the reaction rate on the proton activity (Figure 2e). The dependence of the current density on the phosphate concentration was also evaluated at various water oxidizing potentials. A zeroth-order dependence on the phosphate concentration was observed at each applied potential (Figure 2d). On the basis of the experimental results of the

DOI: 10.1021/jacs.6b10657
J. Am. Chem. Soc. 2017, 139, 2277−2285

electrokinetic analyses, the overall electrochemical rate law for the OER by the MnO NPs was derived, as follows:[48]

$$j = k_0(a_{H^+})^{-1} \exp\left(\frac{FE}{RT}\right) \quad (4)$$

Equation 4 is consistent with a mechanistic sequence involving a quasi-equilibrium reversible $1e^-/1H^+$ transfer step followed by the RDS.[48] Notably, the electrochemical behavior of the MnO NPs under neutral condition is clearly distinct from previously reported Mn-based catalysts, which typically exhibit Tafel slopes of 100−120 mV/dec at neutral pH. For example, commercially available micrometer-sized Mn oxide compounds, MnO_2, Mn_2O_3, and Mn_3O_4, show Tafel slopes of 120 mV/dec and do not exhibit pH dependency.[20] Similar electrochemical data were obtained for the phosphorus-containing materials $Mn_3(PO_4)_2{\cdot}3H_2O$ and $Li_2MnP_2O_7$, which showed Tafel slopes of ∼120 mV/dec.[20,22] Moreover, amorphized Mn oxides also show Tafel slopes of ∼120 mV/dec.[18]

Theoretically, a Tafel slope of 120 mV/dec means that the transfer coefficient (α) in eq 2 is equal to 1/2, which indicates that one-electron oxidation was predicted to be the RDS without a quasi-equilibrium step. Consistent with this speculation, the RDS in the OER by Mn oxides was experimentally identified by in situ spectroscopic analysis of the redox process from Mn(II) to Mn(III).[40,42] Therefore, the distinctive electrokinetic behavior of the MnO NPs may be the reason for their superior OER activity as compared to previously reported Mn catalysts. In addition, the electrokinetic data obtained here did not change as the film thickness increased, indicating that the established electrochemical law can be commonly applied to the reaction kinetics of MnO NPs irrespective of film thickness. For this reason, 300 nm-thick MnO NP films were used for further mechanistic studies.

In the CV curves, unique redox characteristics of the MnO NPs were observed. Specifically, two distinct redox waves appeared at 0.68 and 1.07 V vs NHE, and both redox waves displayed pH-dependent shifts between pH 7 and 8 (Figure 3a). The peak positions of the first and second redox waves shifted at the rate of −77 and −61 mV/pH, respectively. As these values are similar to 59 mV/dec, stepwise proton-coupled oxidations likely occurred before and during the OER. The pH-dependent behavior of the MnO NPs was analogous to that of Co−Pi catalysts under neutral conditions.[52,53] The redox and onset potentials for the OER catalyzed by Co−Pi are shifted negatively at increasing pH. The sequential Co redox waves exhibit a pH dependency similar to those of the MnO NPs.[52,53]

In addition to the redox waves, the onset of Faradaic water oxidation current, which was initiated immediately after the second redox process, was also shifted (Figure 3a). In contrast, the bulk Mn oxides, MnO and Mn_3O_4, exhibited only non-Faradaic current of several $\mu A/cm^2$ (Figure 3b). These electrochemical behaviors were consistent with a previous study reporting that the onset potential of the OER by conventional Mn oxides, such as MnO_2, remains unchanged at pH < 9.[40] Therefore, the sequential proton-coupled redox reactions appear to be specific for the MnO NPs.

To shed light on the redox chemistry of the MnO NPs, spectroscopic analyses were performed to detect reaction intermediates. Continuous wave EPR (CW-EPR) spectroscopy was utilized to monitor the Mn oxidation state of the MnO NPs. The perpendicular and parallel mode EPR spectra of the MnO NPs at the four applied potentials (0.4, 0.75, 1.1, and 1.3 V vs NHE) are presented in Figure 4a. The EPR spectrum of the as-prepared MnO NPs exhibited characteristic Mn(II) (S = 5/2, $g_{eff} \approx 2$) and Mn(III) (S = 2, $g_{eff} \approx 8.2$) signals with a six-line[55]Mn (I = 5/2, 100% abundance) hyperfine splitting in the perpendicular and parallel modes, respectively.

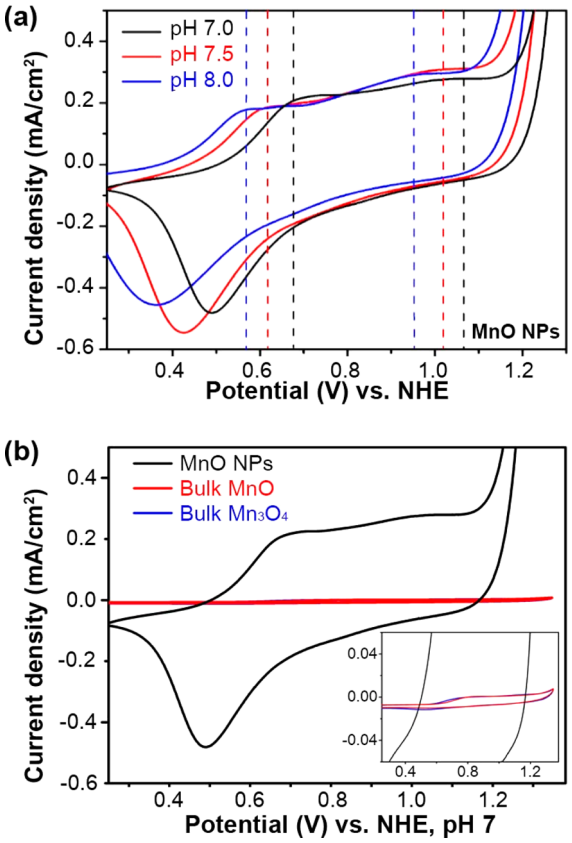

Figure 3. Comparison of the cyclic voltammetry curves of MnO NPs and bulk Mn oxide compounds. (a) pH-dependent redox peak shift of the MnO NPs and (b) comparison of the redox behavior between bulk Mn_3O_4, bulk MnO, and the MnO NPs.

We next quantitatively compared the intensity of the Mn(II)/Mn(III) spectra on the MnO NPs above and below the Mn redox potentials. At potentials near the first redox wave, the Mn(II) signals continuously decreased, whereas the Mn(III) signals were enhanced (Figure 4b). The observed spectral changes and obtained electrochemical data imply that the first redox wave corresponds to Mn(II)−H_2O → Mn(III)−OH.[27] The protonation states of the surface species on the Mn active sites were estimated on the basis of the pK_a values of the hydroxyl groups on Mn(II) and Mn(III) reported as 10.6 and 0.7, respectively.[27,54] At potentials above the second redox wave, Mn(II) signals were no longer detected, and the Mn(III) signals were slightly decreased (Figure 4b). According to a previous EPR study, Mn(V) species in an Mn complex can be detected by the signals at $g \approx 8.5$ in the parallel mode;[55] however, such signals were not observed in the present study. In addition, although Mn(IV) species displayed an EPR signal at $g \approx 4.3$ in the perpendicular mode, it was difficult to directly capture Mn(IV) species because of difficulty in determining the accurate zero field splitting value and rapid decay of reaction intermediates.[56,57] Thus, the present results indirectly support the conclusion that higher Mn valency is generated during catalysis.

DOI: 10.1021/jacs.6b10657
J. Am. Chem. Soc. 2017, 139, 2277−2285

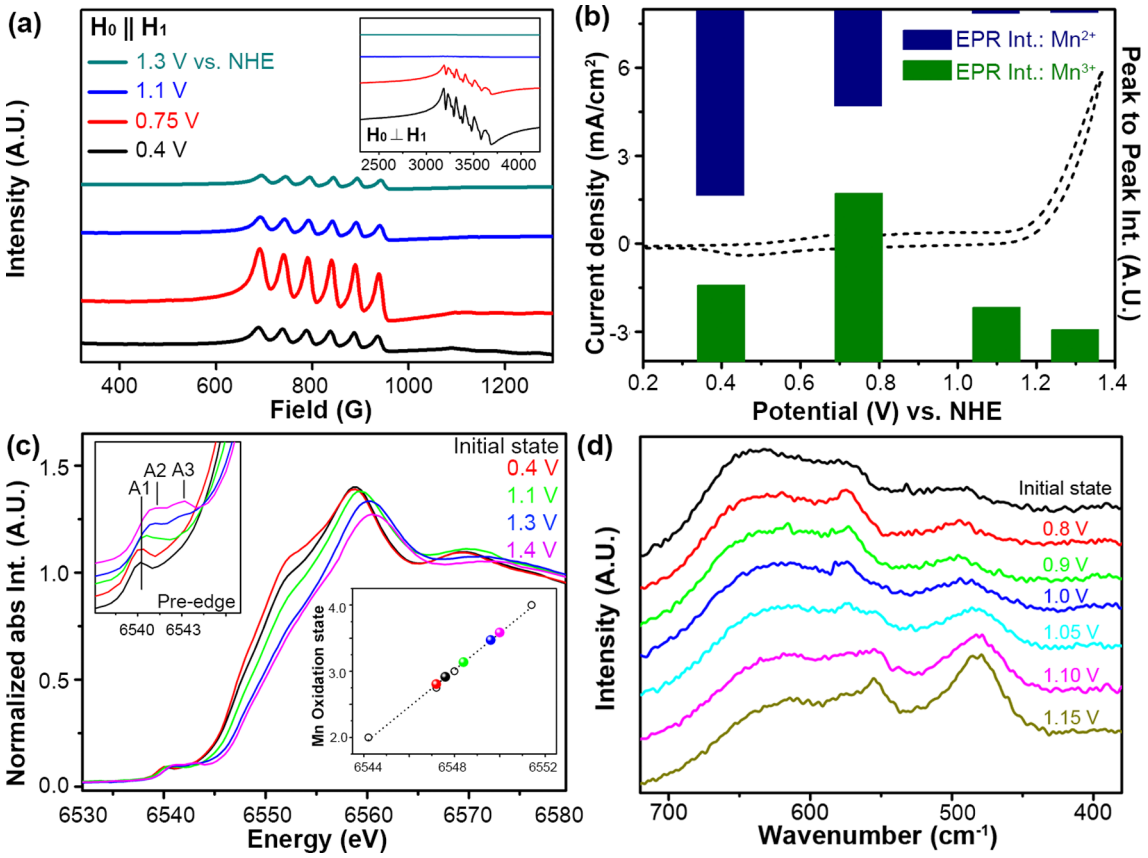

Figure 4. Mn valency change during water oxidation catalysis. (a) Parallel mode X-band CW-EPR spectra (inset: perpendicular mode CW-EPR spectra), (b) peak to peak EPR intensity, (c) Mn K-edge XANES spectra, and the average oxidation state of Mn demonstrating oxidation of Mn to higher valency (inset: the enlarged pre-edge region (left) and the estimated average oxidation state of Mn (right)), and (d) in situ Raman spectra of the MnO NPs. All potential-dependent spectra were collected during bulk electrolysis at the indicated potentials.

The existence of Mn(IV) or Mn(V) species during catalysis was further supported by the results of in situ XANES and EXAFS analysis (Figure S8). For the analysis, pre-electrolysis was conducted at constant potentials to achieve a catalytic steady state. As expected, a clear positive shift was observed in the Mn K-edge spectra with an increase in the applied potential. The average Mn oxidation state was calculated using the spectra of the reference Mn oxide compounds (Figure 4c, inset). The oxidation states in the absence of an applied potential had average values of approximately 2.7, indicating that the valency of Mn was a mixture of Mn(II) and Mn(III). At 0.4 V vs NHE, the average oxidation state was slightly reduced. This decline was attributed to partial reduction of Mn on the surface of the MnO NPs, in accordance with the negative current observed at 0.4 V vs NHE in the CV curves (Figure 3a). Over the open circuit potential, a positive shift was observed in the Mn K-edge spectra. The Mn oxidation states were estimated to be 3.21 and 3.46 at 1.3 and 1.4 V vs NHE, respectively (Figure 4c).

The unique redox change from Mn(II) to Mn(IV) via the formation of Mn(III) was verified by in situ Raman spectroscopy. Raman spectra of the MnO NPs measured during electrolysis at constant potentials are shown in Figure 4d. In the initial state, characteristic Mn(II)−O stretching vibration (A_g) and Mn(III)−O stretching (E_g) modes were observed as broad shoulder bands around 640 and 575 cm^{-1}, respectively.[58,59] As the applied potential increased to 1.05 V vs NHE, where the OER was initiated, new Raman peaks appeared at approximately 555 and 480 cm^{-1}, with a corresponding decrease in intensity of the Mn(III)-related bands.[58,60] In addition, the Raman shift values and relative intensities of the generated peaks were well matched with the stretching vibration of Mn(IV)−O species.[58] The reversibility of the Raman spectra was also confirmed (Figure S7). These observations therefore further demonstrated that the MnO NPs undergo a sequential redox change to form active Mn(IV) species.

The generated reaction intermediates were further identified by in situ diffuse transmission UV−vis analysis. Spectral changes of the MnO NP electrodes caused by the catalytic reaction were monitored at pH 7 between 0.8 and 1.3 V vs NHE in 0.1 V increments. To evaluate the Mn species formed on the surface of the MnO NPs, we additionally obtained differential spectra at each potential by subtraction of the spectra obtained at 0.8 V (Figures 5a and S2). Initially, the MnO NPs exhibited two bands in the UV regions at approximately 350 and 380 nm, corresponding to $O^{2-} \rightarrow Mn^{II}$ and $O^{2-} \rightarrow Mn^{III}$ ligand-to-metal charge transfer, respectively, along with several weak peaks originating from d−d transitions in the visible region.[61] As shown in Figure 5a, upon increasing the applied potentials at 0.1 V increments, two distinct absorption bands in the regions of 400 nm (ΔAbs_{400}) and 600 nm (ΔAbs_{600}) were identified. ΔAbs_{400} showed relatively sharp features, whereas ΔAbs_{600} had a broad and wide shoulder.

The origins of the observed redox peaks were assigned on the basis of the peak characteristics and results of previous studies.

DOI: 10.1021/jacs.6b10657
J. Am. Chem. Soc. 2017, 139, 2277−2285

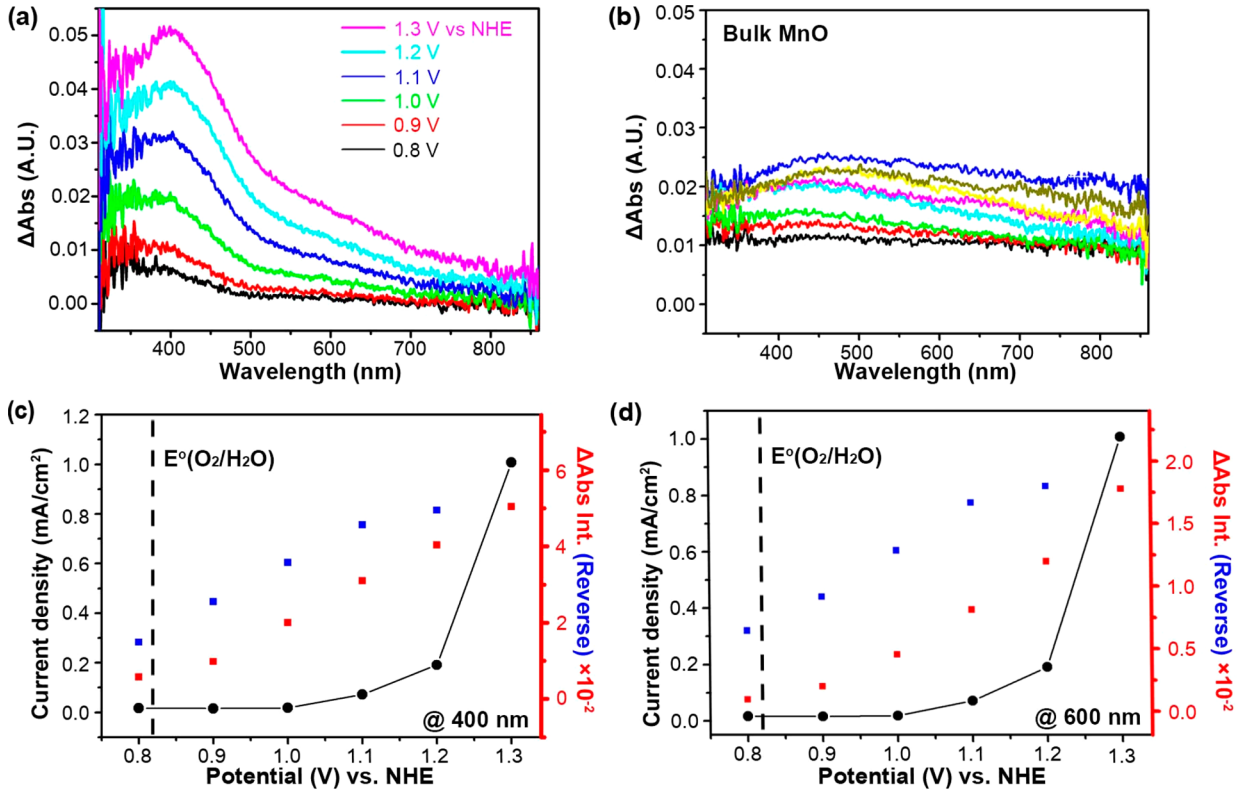

Figure 5. In situ UV−vis spectra of the MnO NPs. (a) Difference spectra based on the applied potential, (b) difference spectra of bulk MnO, and (c,d) potential dependence of the current density (solid line) and differential absorbance at 400 and 600 nm for the MnO NPs.

Mn(III) in Mn_3O_4 nanoparticles reportedly exhibits $O^{2-} \rightarrow Mn^{II}$ (210−250 nm) and $O^{2-} \rightarrow Mn^{III}$ (350−390 nm) charge transfer transitions and d−d crystal field transitions in the range of 550−700 nm.[62−64] In contrast, Mn(IV) species in MnO_2 exhibit a broad peak in the region of 400 nm and shoulder peaks at approximately 575 and 700 nm.[65] The in situ UV−vis spectral changes for the MnO NPs, in which a continuous peak between 350 and 500 nm and a broad shoulder between 500 and 700 nm were observed, are nearly identical to those previously reported for Mn(IV) species in MnO_2 nanocrystals.[66,67] Although no distinct peak was observed for Mn(V), we could not exclude the formation of Mn(V) species during catalysis. However, most Mn(V) species described in the literature exhibit two distinct peaks in the range of 350 and 520 nm.[68] Therefore, ΔAbs_{400} and ΔAbs_{600} likely correspond to Mn(IV) species, rather than Mn(III) or Mn(V) species.

The formation of Mn(IV) species was also further supported by the results of XANES, EPR, and Raman spectral analyses, as described above. Taken together, the findings from the present analyses by the measurement of CV, EPR, XANES, and Raman (Figures 3a and 4) and previous studies examining Mn oxide compounds indicate that ΔAbs_{400} corresponds to the ligand-to-metal charge transfer band of Mn(IV) species.[60,69] Furthermore, ΔAbs_{600} can be assigned to the d−d transition band of Mn(IV). Because the d−d transition of the octahedral system is Laporte forbidden according to the selection rule, the d−d transition band of Mn(IV)−O species intrinsically exhibits broad peak characteristics with low intensity.[70,71]

ΔAbs_{400}, ΔAbs_{600}, and the current density were plotted against applied potentials to the MnO NPs (Figure 5c,d). The intensity of the two absorption peaks was strongly correlated with the onset of the OER. Moreover, the reversibility of the Mn species was also demonstrated. A gradual decline of the peak intensity was detected as the potential was reversed (Figure S4). In contrast, no spectral changes at the same potential range were observed for the bulk MnO compounds (Figures 5b and S3). In addition, no peak changes were detected for the MnO NPs when the in situ experiments were conducted in an organic electrolyte, $(TBA)ClO_4$ in $CHCl_3$ (Figure S5), that was consistent with a previous study.[40] Therefore, it is considered that the observed spectral changes resulted from the formation of Mn(IV)═O species in the presence of water.

Formation of Mn(IV)═O can be observed in pre-edge XANES spectra at high anodic potential as shown in Figure 4c. As the potential increased to 1.4 V vs NHE, a new park around 6543 eV (marked as A3) distinctly emerged. According to previous studies,[72,73] this abnormal feature can be attributed to the formation of Mn(IV)═O. Additionally, potential-dependent EXAFS data also provided the evidence of Mn(IV)═O formation. The bond length of octahedral Mn−O was 1.79 Å at the initial state and low potential (Figure S9). At 1.4 V, the Mn−O bond became shortened to 1.70 Å, which accorded with the characteristic bonding lengths of Mn═O in previous reports.[72,74,75] Taken together, evidence for the generation of the Mn(IV)═O species has been observed.

On the basis of the present electrokinetic and spectroscopic analyses, we constructed a scheme of an overall redox process for Mn species on the MnO NPs during the OER. The observed redox behavior and pH-dependent shifts in the CV curves (Figure 3a), combined with the EPR results (Figure 4a,b), suggest that Mn(II)−H_2O surface species are oxidized to Mn(III)−OH during the first redox wave. The in situ XANES and Raman data (Figure 4c,d) confirmed the stepwise oxidation

DOI: 10.1021/jacs.6b10657
J. Am. Chem. Soc. 2017, 139, 2277−2285

Scheme 1. Proposed Water Oxidation Mechanisms of Conventional Mn Catalysts (top) and the Monodisperse 10 nm-Sized MnO NPs (bottom)[a]

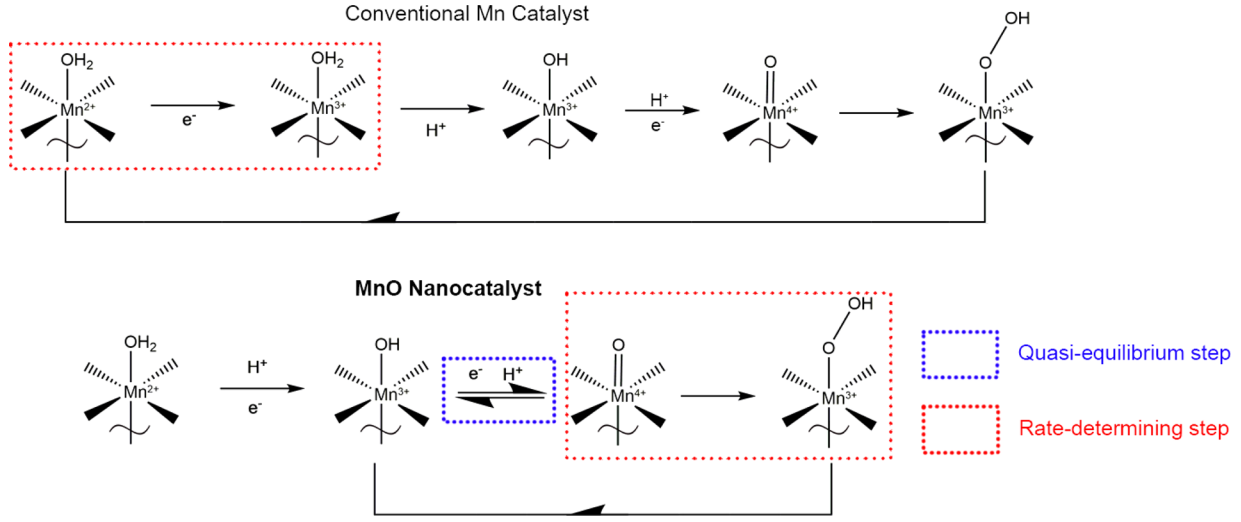

[a]Blue and red dotted rectangles indicate the quasi-equilibrium and rate-determining step, respectively. Each model represents the terminated surface active species including Mn atoms and bound reaction species.

of Mn(II) to Mn(IV) via the formation of Mn(III). Furthermore, the electrokinetic (Figure 2) and in situ UV−vis (Figure 5) data revealed that a concerted one-proton and one-electron oxidation reaction, Mn(III)−OH → Mn(IV)═O, occurred as a quasi-equilibrium step before the RDS.

Finally, we compared the proposed mechanistic schemes of our MnO NPs and conventional Mn catalysts (Scheme 1). As stated above, the RDS for conventional Mn catalysts is a one-electron oxidation reaction, Mn(II)−H_2O → Mn(III)−H_2O, which proceeds without a quasi-equilibrium step. Experimental data for the zeroth reaction order of proton and the transfer coefficient value of 1/2 also support this claim. After formation of Mn(III)−H_2O, sequential deprotonation processes are expected to occur, based on the pK_a value of Mn(III) species.[27] In contrast, for the 10 nm-sized MnO NPs, the formation of Mn(III) species is no longer the RDS. Rather, a concerted proton−electron transfer reaction proceeds as a quasi-equilibrium step to produce Mn(IV)═O intermediates. The reaction mechanism proposed here is displayed on the basis of the spectroscopic and electrokinetic evidence of Mn(IV)═O assuming the AB mechanism (Scheme 1). However, we consider that O−O bond formation after the step of the generation of Mn(IV)═O can be modified or further interpreted based on RC mechanisms,[6,76,77] radical-involved AB mechanisms,[23] or mechanisms involving lattice oxygen.[78]

From this comparative study, we demonstrated that the improved catalytic property of the MnO NPs can be explained by the unique reaction mechanism. Stabilization of Mn(III) intermediates in the MnO NPs appears to alter the RDS. However, further study is required to understand why uniform, assembled NPs exhibit such exceptional behaviors. Recent studies about metal-based NPs may provide new insights into their electrocatalytic properties. Recently, lattice distortion was reported as a distinctive characteristic of nanosized materials.[79] From the X-ray analysis, it was revealed that quantum dot NPs with a diameter less than 10 nm possess lattice distorted surface structure, which results in defective nature.[70] Defects on the surface of NPs can not only enhance electric conductivity, but also change binding energies with reactants and alter electron configurations of metal atoms.[80] Indeed, interplay between the defective nature of oxide materials and the electrocatalytic activity for the oxygen reduction reaction has been demonstrated.[80,81] Moreover, enhanced proton conductivity in the porous catalyst film and the stabilization of high-index facets on the surface can also be possible origins of the nanosize effects on the catalytic activity.[52,53,79] In this regard, we believe that methodical investigation using computation analyses will aid in the understanding of nanosize effects on the catalytic behavior and enable the improved design of OER catalysts.

■ CONCLUSIONS

We investigated the electrochemical water oxidizing mechanism mediated by the MnO NPs and revealed that this material exhibits exceptionally high catalytic activity under neutral conditions. Comprehensive electrochemical and spectroscopic analyses demonstrated that the nanosized Mn oxide electrocatalyst was mechanistically distinct from conventional Mn catalysts. Specifically, a concerted one-proton and one-electron transfer occurs as the quasi-equilibrium step, followed by a chemical RDS. The sequential oxidation of Mn and generation of Mn(IV)═O species were directly monitored by various spectroscopic analyses, including EPR, in situ XANES, UV−vis, and Raman spectroscopy, by virtue of a high surface-area-to-volume ratio of the MnO NPs. We believe that the unique water-oxidizing mechanism of the MnO NPs is attributed to the high catalytic activity of this material for the OER at neutral pH.

■ ASSOCIATED CONTENT

Supporting Information

The Supporting Information is available free of charge on the ACS Publications website at DOI: 10.1021/jacs.6b10657.

Full experimental methods and Figures S1−S9 (PDF)

■ AUTHOR INFORMATION

Corresponding Authors

*ryuhei.nakamura@riken.jp

*nkitae@snu.ac.kr

DOI: 10.1021/jacs.6b10657
J. Am. Chem. Soc. 2017, 139, 2277−2285

ORCID

Sun Hee Kim: 0000-0001-6557-1996
Ryuhei Nakamura: 0000-0003-0743-8534
Ki Tae Nam: 0000-0001-6353-8877

Author Contributions

[#]K.J., H.S., and T.H. contributed equally.

Notes

The authors declare no competing financial interest.

■ ACKNOWLEDGMENTS

This research was supported by the Global Frontier R&D Program of the Center for Multiscale Energy System funded by the National Research Foundation under the Ministry of Science, ICT & future, Korea (2011-0031571), KIST Institutional Program (0543-20160004), by the Ministry of Trade, Industry & Energy (MOTIE) under Industrial Strategic Technology Development Program, Korea (0417-2016-0019), and Research Institute of Advanced Materials (RIAM) at Seoul National University to K.T.N. and the C1 Gas Refinery Program through the NRF funded by the Ministry of Science, ICT & Future Planning (2015M3D3A1A01064876), to S.H.K. This work was also supported by JSPS Grant-in-Aid for Scientific Research No. 26288092 to R.N. T.H. acknowledges Grant-in-Aid for JSPS Fellows No. 15J10583.

■ REFERENCES

(1) Dresselhaus, M. S.; Thomas, I. L. *Nature* **2001**, *414*, 332.
(2) Bockris, J. O. M.; Veziroglu, T. N. *Int. J. Hydrogen Energy* **2007**, *32*, 1605.
(3) Man, I. C.; Su, H.-Y.; Calle-Vallejo, F.; Hansen, H. A.; Martínez, J. I.; Inoglu, N. G.; Kitchin, J.; Jaramillo, T. F.; Nørskov, J. K.; Rossmeisl, J. *ChemCatChem* **2011**, *3*, 1159.
(4) Dau, H.; Limberg, C.; Reier, T.; Risch, M.; Roggan, S.; Strasser, P. *ChemCatChem* **2010**, *2*, 724.
(5) McCrory, C. C. L.; Jung, S.; Peters, J. C.; Jaramillo, T. F. *J. Am. Chem. Soc.* **2013**, *135*, 16977.
(6) Duan, L.; Bozoglian, F.; Mandal, S.; Stewart, B.; Privalov, T.; Llobet, A.; Sun, L. *Nat. Chem.* **2012**, *4*, 418.
(7) Yagi, M.; Tomita, E.; Sakita, S.; Kuwabara, T.; Nagai, K. *J. Phys. Chem. B* **2005**, *109*, 21489.
(8) Smith, R. D. L.; Sporinova, B.; Fagan, R. D.; Trudel, S.; Berlinguette, C. P. *Chem. Mater.* **2014**, *26*, 1654.
(9) Kanan, M. W.; Nocera, D. G. *Science* **2008**, *321*, 1072.
(10) Kim, H.; Park, J.; Park, I.; Jin, K.; Jerng, S. E.; Kim, S. H.; Nam, K. T.; Kang, K. *Nat. Commun.* **2015**, *6*, 8253.
(11) Liang, Y.; Li, Y.; Wang, H.; Zhou, J.; Wang, J.; Regier, T.; Dai, H. *Nat. Mater.* **2011**, *10*, 780.
(12) Fillol, J. L.; Codolà, Z.; Garcia-Bosch, I.; Gómez, L.; Pla, J. J.; Costas, M. *Nat. Chem.* **2011**, *3*, 807.
(13) Okamura, M.; Kondo, M.; Kuga, R.; Kurashige, Y.; Yanai, T.; Hayami, S.; Praneeth, V. K. K.; Yoshida, M.; Yoneda, K.; Kawata, S.; Masaoka, S. *Nature* **2016**, *530*, 465.
(14) Chowdhury, D. R.; Spiccia, L.; Amritphale, S. S.; Paul, A.; Singh, A. *J. Mater. Chem. A* **2016**, *4*, 3655.
(15) Roger, I.; Symes, M. D. *J. Am. Chem. Soc.* **2015**, *137*, 13980.
(16) Bediako, D. K.; Lassalle-Kaiser, B.; Surendranath, Y.; Yano, J.; Yachandra, V. K.; Nocera, D. G. *J. Am. Chem. Soc.* **2012**, *134*, 6801.
(17) Indra, A.; Menezes, P. W.; Zaharieva, I.; Baktash, E.; Pfrommer, J.; Schwarze, M.; Dau, H.; Driess, M. *Angew. Chem., Int. Ed.* **2013**, *52*, 13206.
(18) Huynh, M.; Shi, C.; Billinge, S. J.; Nocera, D. G. *J. Am. Chem. Soc.* **2015**, *137*, 14887.
(19) Bergmann, A.; Zaharieva, I.; Dau, H.; Strasser, P. *Energy Environ. Sci.* **2013**, *6*, 2745.
(20) Jin, K.; Park, J.; Lee, J.; Yang, K. D.; Pradhan, G. K.; Sim, U.; Jeong, D.; Jang, H. L.; Park, S.; Kim, D.; Sung, N.-E.; Kim, S. H.; Han, S.; Nam, K. T. *J. Am. Chem. Soc.* **2014**, *136*, 7435.
(21) Hocking, R. K.; Brimblecombe, R.; Chang, L.-Y.; Singh, A.; Cheah, M. H.; Glover, C.; Casey, W. H.; Spiccia, L. *Nat. Chem.* **2011**, *3*, 461.
(22) Park, J.; Kim, H.; Jin, K.; Lee, B. J.; Park, Y.-S.; Kim, H.; Park, I.; Yang, K. D.; Jeong, H.-Y.; Kim, J.; Hong, K. T.; Jang, H. W.; Kang, K.; Nam, K. T. *J. Am. Chem. Soc.* **2014**, *136*, 4201.
(23) Huynh, M.; Bediako, D. K.; Nocera, D. G. *J. Am. Chem. Soc.* **2014**, *136*, 6002.
(24) Lee, S. W.; Carlton, C.; Risch, M.; Surendranath, Y.; Chen, S.; Furutsuki, S.; Yamada, A.; Nocera, D. G.; Shao-Horn, Y. *J. Am. Chem. Soc.* **2012**, *134*, 16959.
(25) Suga, M.; Akita, F.; Hirata, K.; Ueno, G.; Murakami, H.; Nakajima, Y.; Shimizu, T.; Yamashita, K.; Yamamoto, M.; Ago, H.; Shen, J.-R. *Nature* **2014**, *517*, 99.
(26) Galstyan, A.; Robertazzi, A.; Knapp, E. W. *J. Am. Chem. Soc.* **2012**, *134*, 7442.
(27) Yamaguchi, A.; Inuzuka, R.; Takashima, T.; Hayashi, T.; Hashimoto, K.; Nakamura, R. *Nat. Commun.* **2014**, *5*, 4256.
(28) Morita, M.; Iwakura, C.; Tamura, H. *Electrochim. Acta* **1979**, *24*, 357.
(29) Morita, M.; Iwakura, C.; Tamura, H. *Electrochim. Acta* **1977**, *22*, 325.
(30) Mohammad, A. M.; Awad, M. I.; El-Deab, M. S.; Okajima, T.; Ohsaka, T. *Electrochim. Acta* **2008**, *53*, 4351.
(31) Zaharieva, I.; Chernev, P.; Risch, M.; Klingan, K.; Kohlhoff, M.; Fischer, A.; Dau, H. *Energy Environ. Sci.* **2012**, *5*, 7081.
(32) Robinson, D. M.; Go, Y. B.; Mui, M.; Gardner, G.; Zhang, Z.; Mastrogiovanni, D.; Garfunkel, E.; Li, J.; Greenblatt, M.; Dismukes, G. C. *J. Am. Chem. Soc.* **2013**, *135*, 3494.
(33) Suntivich, J.; May, K. J.; Gasteiger, H. A.; Goodenough, J. B.; Shao-Horn, Y. *Science* **2011**, *334*, 1383.
(34) Vojvodic, A.; Nørskov, J. K. *Science* **2011**, *334*, 1355.
(35) Yagi, S.; Yamada, I.; Tsukasaki, H.; Seno, A.; Murakami, M.; Fujii, H.; Chen, H.; Umezawa, N.; Abe, H.; Nishiyama, N.; Mori, S. *Nat. Commun.* **2015**, *6*, 8249.
(36) Zhang, M.; de Respinis, M.; Frei, H. *Nat. Chem.* **2014**, *6*, 362.
(37) Gerken, J. B.; McAlpin, J. G.; Chen, J. Y. C.; Rigsby, M. L.; Casey, W. H.; Britt, R. D.; Stahl, S. S. *J. Am. Chem. Soc.* **2011**, *133*, 14431.
(38) Wang, L.-P.; Van Voorhis, T. *J. Phys. Chem. Lett.* **2011**, *2*, 2200.
(39) Betley, T. A.; Surendranath, Y.; Childress, M. V.; Alliger, G. E.; Fu, R.; Cummins, C. C.; Nocera, D. G. *Philos. Trans. R. Soc., B* **2008**, *363*, 1293.
(40) Takashima, T.; Hashimoto, K.; Nakamura, R. *J. Am. Chem. Soc.* **2012**, *134*, 18153.
(41) Mazin, I.; Khomskii, D.; Lengsdorf, R.; Alonso, J.; Marshall, W.; Ibberson, R.; Podlesnyak, A.; Martinez-Lope, M.; Abd-Elmeguid, M. *Phys. Rev. Lett.* **2007**, *98*, 176406.
(42) Takashima, T.; Yamaguchi, A.; Hashimoto, K.; Irie, H.; Nakamura, R. *Electrochemistry* **2014**, *82*, 325.
(43) Najafpour, M. M.; Sedigh, D. J. *Dalton Trans.* **2013**, *42*, 12173.
(44) Najafpour, M. M.; Haghighi, B.; Sedigh, D. J.; Ghobadi, M. Z. *Dalton Trans.* **2013**, *42*, 16683.
(45) Kuo, C. H.; Li, W.; Pahalagedara, L.; El-Sawy, A. M.; Kriz, D.; Genz, N.; Guild, C.; Ressler, T.; Suib, S. L.; He, J. *Angew. Chem., Int. Ed.* **2015**, *54*, 2345.
(46) Jin, K.; Chu, A.; Park, J.; Jeong, D.; Jerng, S. E.; Sim, U.; Jeong, H.-Y.; Lee, C. W.; Park, Y.-S.; Yang, K. D.; Pradhan, G. K.; Kim, D.; Sung, N.-E.; Kim, S. H.; Nam, K. T. *Sci. Rep.* **2015**, *5*, 10279.
(47) Jeong, D.; Jin, K.; Jerng, S. E.; Seo, H.; Kim, D.; Nahm, S. H.; Kim, S. H.; Nam, K. T. *ACS Catal.* **2015**, *5*, 4624.
(48) Bard, A. J.; Faulkner, L. *Electrochemical Techniques: Fundamentals and Applications*; Wiley and Sons: New York, 1980.
(49) Doyle, R. L.; Godwin, I. J.; Brandon, M. P.; Lyons, M. E. G. *Phys. Chem. Chem. Phys.* **2013**, *15*, 13737.

DOI: 10.1021/jacs.6b10657
J. Am. Chem. Soc. 2017, 139, 2277−2285

(50) Surendranath, Y.; Kanan, M. W.; Nocera, D. G. *J. Am. Chem. Soc.* **2010**, *132*, 16501.
(51) Shinagawa, T.; Garcia-Esparza, A. T.; Takanabe, K. *Sci. Rep.* **2015**, *5*, 13801.
(52) Bediako, D. K.; Costentin, C.; Jones, E. C.; Nocera, D. G.; Savéant, J.-M. *J. Am. Chem. Soc.* **2013**, *135*, 10492.
(53) Costentin, C.; Porter, T. R.; Savéant, J.-M. *J. Am. Chem. Soc.* **2016**, *138*, 5615.
(54) Hawkes, S. J. *J. Chem. Educ.* **1996**, *73*, 516.
(55) Gupta, R.; Taguchi, T.; Lassalle-Kaiser, B.; Bominaar, E. L.; Yano, J.; Hendrich, M. P.; Borovik, A. S. *Proc. Natl. Acad. Sci. U. S. A.* **2015**, *112*, 5319.
(56) Zlatar, M.; Gruden, M.; Vassilyeva, O. Y.; Buvaylo, E. A.; Ponomarev, A.; Zvyagin, S.; Wosnitza, J.; Krzystek, J.; Garcia-Fernandez, P.; Duboc, C. *Inorg. Chem.* **2016**, *55*, 1192.
(57) Kim, S. H.; Park, H.; Seo, M. S.; Kubo, M.; Ogura, T.; Klajn, J.; Gryko, D. T.; Valentine, J. S.; Nam, W. *J. Am. Chem. Soc.* **2010**, *132*, 14030.
(58) Julien, C.; Massot, M.; Baddour-Hadjean, R.; Franger, S.; Bach, S.; Pereira-Ramos, J. P. *Solid State Ionics* **2003**, *159*, 345.
(59) Dubal, D. P.; Dhawale, D. S.; Salunkhe, R. R.; Pawar, S. M.; Lokhande, C. D. *Appl. Surf. Sci.* **2010**, *256*, 4411.
(60) Hao, X.; Zhao, J.; Li, Y.; Zhao, Y.; Ma, D.; Li, L. *Colloids Surf., A* **2011**, *374*, 42.
(61) Wells, C. F.; Davies, G. *J. Chem. Soc. A* **1967**, 1858.
(62) Yu, W.; Zhou, C.; Tong, D.; Xu, T. *J. Mol. Catal. A: Chem.* **2012**, *365*, 194.
(63) Chen, S.; Zhu, J.; Wu, X.; Han, Q.; Wang, X. *ACS Nano* **2010**, *4*, 2822.
(64) Al-Oweini, R.; Sartorel, A.; Bassil, B. S.; Natali, M.; Berardi, S.; Scandola, F.; Kortz, U.; Bonchio, M. *Angew. Chem., Int. Ed.* **2014**, *53*, 11182.
(65) Sakai, N.; Ebina, Y.; Takada, K.; Sasaki, T. *J. Phys. Chem. B* **2005**, *109*, 9651.
(66) Omomo, Y.; Sasaki, T.; Wang, L.; Watanabe, M. *J. Am. Chem. Soc.* **2003**, *125*, 3568.
(67) Butterfield, C. N.; Soldatova, A. V.; Lee, S.-W.; Spiro, T. G.; Tebo, B. M. *Proc. Natl. Acad. Sci. U. S. A.* **2013**, *110*, 11731.
(68) Hong, S.; Lee, Y.-M.; Sankaralingam, M.; Vardhaman, A. K.; Park, Y. J.; Cho, K.-B.; Ogura, T.; Sarangi, R.; Fukuzumi, S.; Nam, W. *J. Am. Chem. Soc.* **2016**, *138*, 8523.
(69) Siebecker, M.; Madison, A. S.; Luther, G. W. *Aquat. Geochem.* **2015**, *21*, 143.
(70) Lever, A. B. P. *Inorganic Electronic Spectroscopy*; Elsevier: Amsterdam; New York, 1984.
(71) Huheey, J. E.; Keiter, E. A.; Keiter, R. L.; Medhi, O. K. *Inorganic Chemistry: Principles of Structure and Reactivity*; Pearson Education, 2006.
(72) Leto, D. F.; Jackson, T. A. *Inorg. Chem.* **2014**, *53*, 6179.
(73) Weng, T.-C.; Hsieh, W.-Y.; Uffelman, E. S.; Gordon-Wylie, S. W.; Collins, T. J.; Pecoraro, V. L.; Penner-Hahn, J. E. *J. Am. Chem. Soc.* **2004**, *126*, 8070.
(74) Kurahashi, T.; Kikuchi, A.; Tosha, T.; Shiro, Y.; Kitagawa, T.; Fujii, H. *Inorg. Chem.* **2008**, *47*, 1674.
(75) Wu, X.; Seo, M. S.; Davis, K. M.; Lee, Y.-M.; Chen, J.; Cho, K.-B.; Pushkar, Y. N.; Nam, W. *J. Am. Chem. Soc.* **2011**, *133*, 20088.
(76) Ray, K.; Heims, F.; Schwalbe, M.; Nam, W. *Curr. Opin. Chem. Biol.* **2015**, *25*, 159.
(77) Casadevall, C.; Codolà, Z.; Costas, M.; Lloret-Fillol, J. *Chem. - Eur. J.* **2016**, *22*, 10111.
(78) Mefford, J. T.; Rong, X.; Abakumov, A. M.; Hardin, W. G.; Dai, S.; Kolpak, A. M.; Johnston, K. P.; Stevenson, K. J. *Nat. Commun.* **2016**, *7*, 11053.
(79) Bertolotti, F.; Dirin, D. N.; Ibáñez, M.; Krumeich, F.; Cervellino, A.; Frison, R.; Voznyy, O.; Sargent, E. H.; Kovalenko, M. V.; Guagliardi, A. *Nat. Mater.* **2016**, *15*, 987.
(80) Yang, T.-Y.; Kang, H.-Y.; Sim, U.; Lee, Y.-J.; Lee, J.-H.; Koo, B.; Nam, K. T.; Joo, Y.-C. *Phys. Chem. Chem. Phys.* **2013**, *15*, 2117.
(81) Cheng, F.; Zhang, T.; Zhang, Y.; Du, J.; Han, X.; Chen, J. *Angew. Chem., Int. Ed.* **2013**, *52*, 2474.

DOI: 10.1021/jacs.6b10657
J. Am. Chem. Soc. 2017, 139, 2277−2285